High-Gain Tapered Long Slot Array for Satcom Applications in PCB Technology with Folded Corporate Feed Network

Adham Mahmoud, Mauro Ettorre, Ronan Sauleau

High-Gain Tapered Long Slot Array for Satcom Applications in PCB Technology with Folded Corporate Feed Network

Adham Mahmoud, *Member, IEEE,* Mauro Ettorre, *Fellow, IEEE,* and Ronan Sauleau, *Fellow, IEEE*

***Abstract*—This paper presents an antenna covering the full frequency band from 17 GHz to 31 GHz for K/Ka-band satellite communication (Satcom) applications. A long slot array with 64 slots is designed for the radiating aperture. It is fed by a tapered corporate feed network (CFN) to reduce the sidelobe level (SLL) in the radiating plane orthogonal to the slots. A new technique to fold the CFN by a factor up to 65% is introduced without affecting the array performance. This technique can be applied to any CFN in a multi-layer system. Both parts are fabricated in printed circuit board (PCB) technology. A pillbox beamformer is used to illuminate the CFN. This beamformer consists of an H-plane horn located in the focal plane of an integrated parabolic reflector. The main beam of the antenna can be steered along the slot plane to provide a ±42° coverage in elevation by changing the position of the horn in the focal plane. The pillbox beamformer is made of Aluminum to minimize losses and is fabricated by computer numerically controlled (CNC) milling. The total size of the antenna is $44.5\times33.1\times4.3\lambda_0^3$ where λ_0 is the wavelength at the maximum frequency of operation (31 GHz).**

***Index Terms*—Long slot, satellite communication (Satcom), printed circuit board (PCB), ultra-low profile, wideband.**

I. Introduction

SATELLITE industry has garnered considerable attention with the promise to offer global coverage and high data rate communication worldwide [1], [2]. In particular, the development of mega constellations in Low Earth Orbit (LEO) at Ku and K/Ka bands is paving the way to new commercial Satcom services. Specifically, the K/Ka bands reserved for Satcom services for both civil and military applications are 17.7-21.2 GHz and 27.5-31 GHz for the down-link and up-link channels, respectively.

Satcom antennas operating at K/Ka bands must meet stringent performance requirements to ensure reliable communications and efficient spectrum utilization. These requirements include high gain and efficiency, low sidelobe levels (SLLs), and wide field of view. Additionally, circular polarization (CP) is essential to enhance link reliability and robustness for long-range signal transmissions.

Conventional parabolic antennas with mechanical beam-steering in both azimuth and elevation are a popular solution due to their low cost and high gain [3], [4]. However, these antennas are bulky and cannot be easily integrated in moving platforms such as trains, airplanes, etc. Solutions that combine a passive and flat antenna system such as a transmitarray or a slotted waveguide antenna array with mechanical beam-steering are also available in literature [5]–[7]. However, these solutions suffer from limited bandwidth to cover the down-link and up-link frequency bands simultaneously. Moreover, the focal length to diameter (F/D) ratio in a transmitarray imposes a restriction on the profile of the antenna.

Other solutions are based on phased arrays and their implementation at K/Ka-band may pose serious integration challenges due to the high number of the monolithic microwave integrated circuits (MMIC) required for their operation [8]–[10]. Additionally, these arrays require high power, which can limit their use in applications where power consumption is critical.

Lately, long slot arrays have become a popular choice for Satcom antennas due to their superior broadband, low profile, and wide-angle scanning capabilities [11]–[14]. These arrays use one radiating aperture to cover the full K/Ka-band for transmission and reception [15]–[17], and when combined with a quasi-optical system, they offer mechanically or electronically controlled elevation beam steering and 2-D scanning via azimuthal rotation of the user terminal [18]–[20]. While long slot arrays are inherently linearly-polarized, recent studies have proposed a solution that achieves circular and dual-linear polarizations by operating the radiating slots in a multi-mode fashion with an engineered dispersion of the parallel-plate corporate feed network (CFN) [21]–[23].

A simpler yet powerful solution is to combine a linearly polarized long slot array with a dual-band polarizer placed near the antenna aperture. This approach offers circular polarization with high isolation between the two frequency bands and enables efficient use of the spectrum without compromising the performance and the bandwidth of the long slot antenna. The dual-band polarizer can be realized using simple and low-cost techniques [24]–[26].

This work focuses on the design of the linearly-polarized long slot array and its integration with a very broadband pillbox beamformer to cover with a single aperture the K/Ka band of Satcom applications over a large field of view (±42° in elevation). Compared to our previous works [11], [14], [16], we present a novel design of a 64-slots tapered long slot array with a minimum measured gain of 30.8 dBi at 19.5 GHz. The long slot array is fabricated using PCB technology, while the

This was carried out while Adham Mahmoud was with with Univ Rennes, CNRS, Institut d'Electronique et des Technologies du numéRique (IETR) – UMR 6164, F-35000, Rennes, France. He is now an RF engineer at Greenerwave, 75002 Paris, France (e-mail: adham.mahmoud@greenerwave.com).

Mauro Ettorre and Ronan Sauleau are with with Univ Rennes, CNRS, Institut d'Electronique et des Technologies du numéRique (IETR) – UMR 6164, F-35000, Rennes, France.

Manuscript received July xy, 2023; revised August yz, 2023.

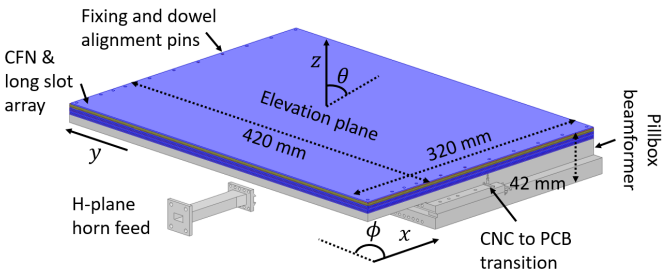

Fig. 1. Perspective view of the antenna (the radiating aperture is made of 64 radiating slots, not shown here).

pillbox beamformer is fabricated by CNC milling. To the best of our knowledge, the proposed pillbox beamformer exhibits the widest impedance bandwidth reported so far. Moreover, we introduce a new technique to design a folded CFN while keeping its true time delay operation that reduces the number of substrate layers for the CFN from 20 to only 7 layers, resulting in a 65% reduction in number of substrate layers and consequently in fabrication costs.

The paper is organized as follows. In Section II, the antenna architecture is presented and each building block of the antenna is described and numerically validated. In Section III, a prototype is presented and validated by measurements. Section IV concludes the paper.

II. Antenna Structure and Operation

Fig. 1 provides a perspective view of the proposed antenna architecture, whereas Fig. 2 graphically introduces the five building blocks of the antenna. These building blocks include an array of 64 long slots, a tapered CFN, a pillbox beamformer, a transition connecting the pillbox beamformer and the CFN, and a novel folding concept referred to as "stair transition", which is applied to both the aforementioned transition and the CFN. Fig. 3 shows a cross-section view of most of the systems and sub-systems shown in the schematic view of Fig. 2. These systems are discussed in details in the following sub-sections along with their corresponding simulation results. Fig. 4 shows the full simulated system combining all the building blocks and discussed later in Section III.

A. Pillbox Beamformer

Fig. 5 presents the pillbox beamformer, a well-reported component in the literature. Its design procedure is available in several references, including [27]–[29]. Here, the pillbox has a focal length of $17\lambda_0$ and a diameter of $44.5\lambda_0$, where λ_0 represents the wavelength at 31 GHz. It is fed by an H-plane sectoral horn and designed to exhibit a –10 dB edge tapering at 17 GHz. The pillbox beam former is designed to control the SLL of the whole antenna along the H-plane (zy-plane in Fig. 1) to a level lower than –20 dB. By displacing the horn in the y-direction, beam steering can be achieved, with a maximum steering angle of approximately 65° when the horn is placed at the pillbox edge. Reflection coefficients up to 60° are provided and far-field radiation patterns up to 42° are presented in the paper.

The pillbox coupler is realized by two 90° symmetrical bends as depicted in Fig. 6. By using three separate metallic plates with a minimum thickness of 3.556mm and a separation of 3.556mm between each metallic plate, a monomodal parallel plate waveguide (PPW) is created. The separation between the metallic plates matches the height of the input standard waveguide WR28 at the Ka-band.

The assembly of the plates is done by screws and dowel alignment pins, with an expected air gap between metallic plates lower than 0.1mm (g_s in Fig. 6). Chokes are introduced to minimize leakage losses. The optimization of the 90° bents is carried out using CST Microwave Studio [30]. The reflection coefficient is better than –35 dB over the entire frequency range from 17 GHz to 31 GHz. To our best knowledge, this is the widest band reported for pillbox couplers. To investigate the effect of the air gap g_s, a parametric sweep has been conducted with a step of 0.01mm, from 0 to 0.1mm. Perfect electric conductors (PEC) are used in simulations to estimate the leakage losses. The results (not given here for brevity) show that the leakage loss remains below 0.1 dB, and the reflection coefficient is unaffected. We have used aluminum for the plates in fabrication.

To feed the horn in the up-link frequency band, a standard waveguide WR28 is utilized with a height of 3.556mm and thus no matching sections are required. In contrast, for the down-link frequency band, a standard waveguide WR51 is employed, which is matched to the PPW structure via three waveguide sections. The system performance is illustrated in Fig. 7, with a reflection coefficient better than –33 dB from 17 to 21.5 GHz. In future works, a diplexer could be implemented to feed the horn through two standard waveguides in parallel [31], [32].

B. Pillbox Beamformer-to-CFN Transition

A transition with wideband capabilities is required to connect the pillbox beamformer and the CFN. Existing literature presents a system design in [33], which exhibits wideband performance ranging from 65 GHz to 87 GHz, with a nearly 30% –10 dB bandwidth. This system [33] does not allow to reach the targeted 55% bandwidth (from 17 GHz to 31 GHz). To address this challenge, a novel transition is proposed, as depicted in Fig. 3a. It consists of various matching sections in both the pillbox coupler and CFN. The matching sections are realised by milling in the metallic layers, whereas by etching and through vias in the substrate layers. The transition requires 4 substrate layers, and no metallic contact is necessary between any of them, reducing fabrication complexity. The used substrate layers are 0.76mm-thick, and are based on ISOLA Astra® MT77 (ϵ_r = 3, tan δ = 0.0013 @ 10 GHz) [34].

The two systems are vertically cascaded on top of each other. An alignment accuracy better than ±25µm is considered during the design. The leakage loss is less than 0.1 dB for a 0.1mm air gap between the PCB and the pillbox beamformer output as well. The reflection coefficient of the transition is represented in Fig. 8, demonstrating a reflection coefficient better than –25 dB across the entire frequency band from 17 to 31 GHz.

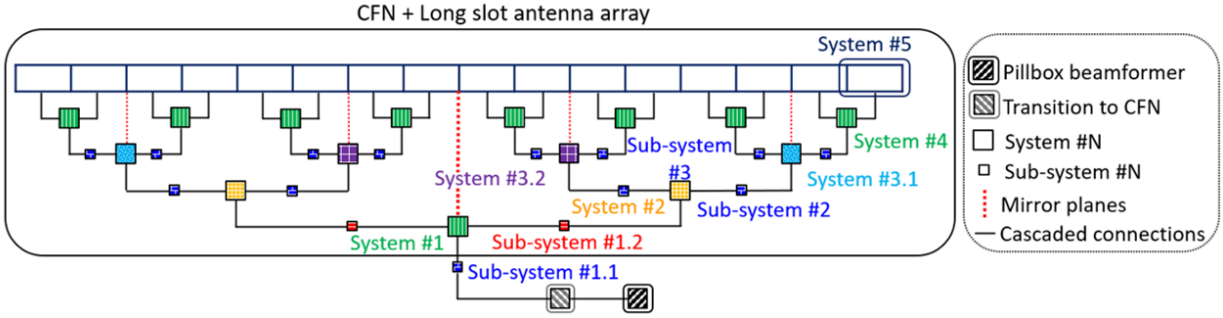

Fig. 2. Full system schematic.

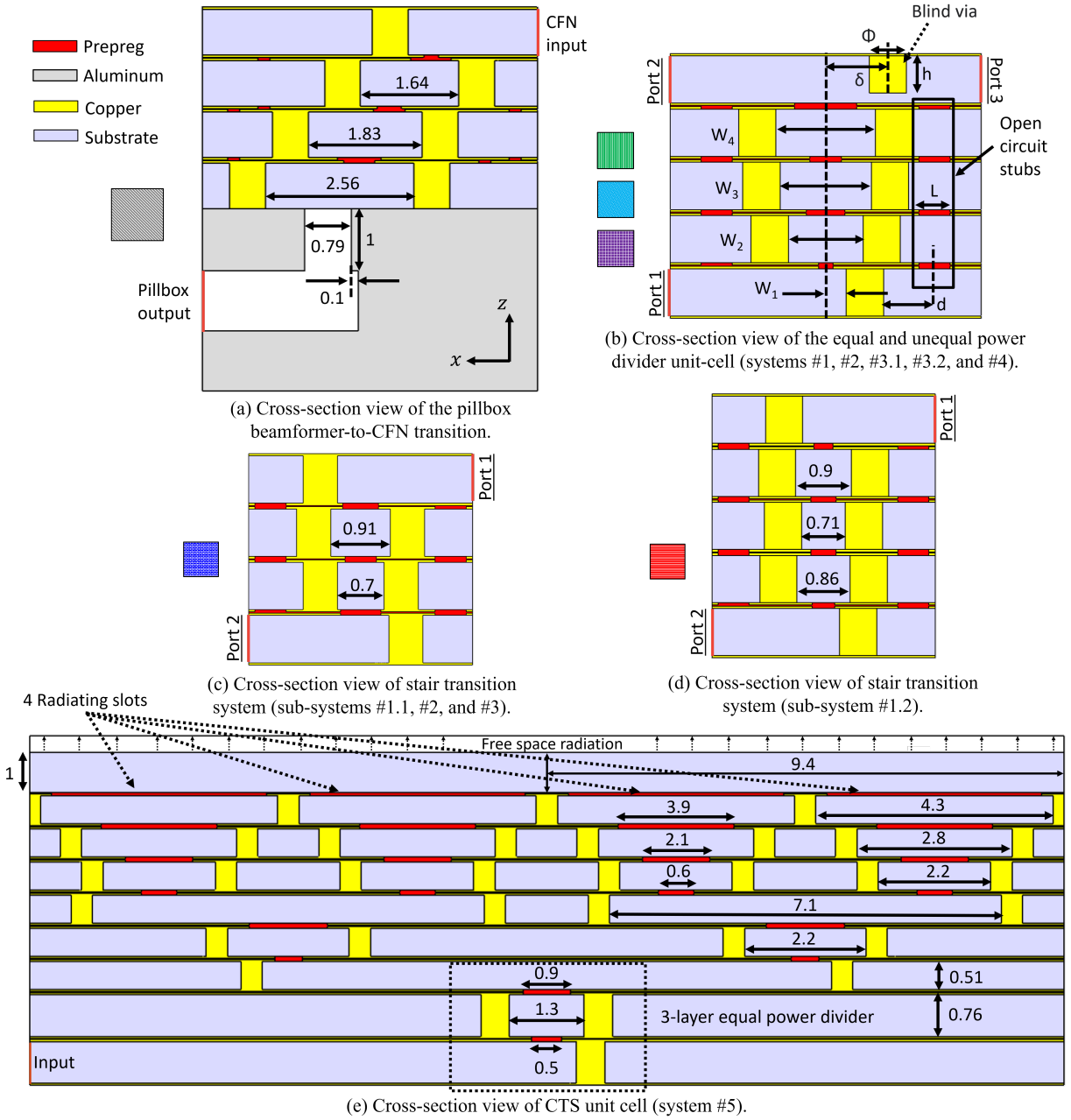

(a) Cross-section view of the pillbox beamformer-to-CFN transition.

(b) Cross-section view of the equal and unequal power divider unit-cell (systems #1, #2, #3.1, #3.2, and #4).

(c) Cross-section view of stair transition system (sub-systems #1.1, #2, and #3).

(d) Cross-section view of stair transition system (sub-system #1.2).

(e) Cross-section view of CTS unit cell (system #5).

Fig. 3. Systems and sub-systems building blocks. All dimensions are in millimeters.

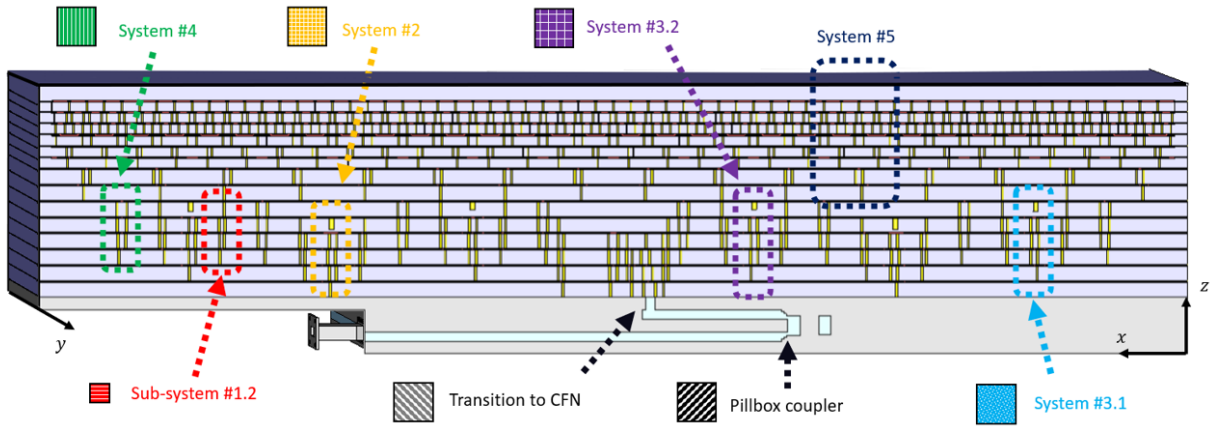

Fig. 4. Reduced 3-D system view (dimensions are not to scale). Please note that the CFN and long slot array are uniform along the y-axis and a single slice of such part may be used to retrieve their performance.

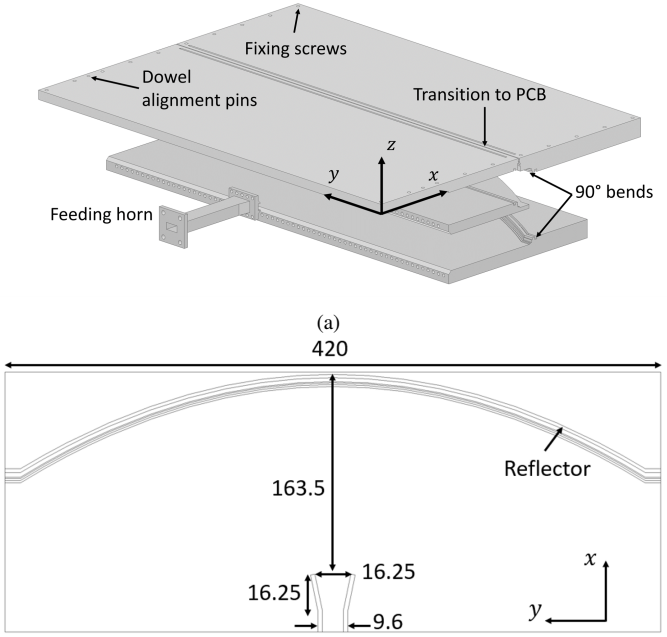

Fig. 5. Geometry and dimensions of the pillbox beamformer. All dimensions are in millimeters. (a) Exploded view. (b) Schematic view.

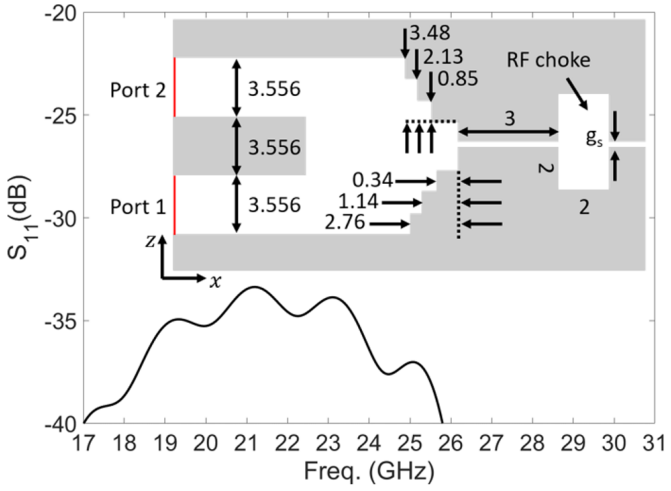

Fig. 6. Dimensions and simulated reflection coefficient of the pillbox coupler. All dimensions are in millimeters.

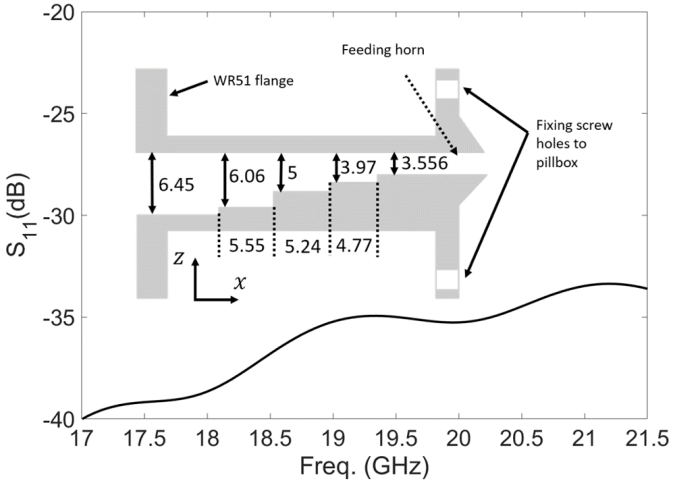

Fig. 7. WR51 standard waveguide matching section to horn input. All dimensions are in millimeters.

C. Corporate Feed Network (CFN)

The CFN is vital for a tapered long slot antenna array, particularly for Satcom applications where achieving a low SLL in the up-link frequency band is crucial to minimize signal interference with other satellites. In this context, 64 slots serve as the radiating aperture of the antenna. While a classical Taylor excitation could be employed to excite the array and ensure the required SLL, such a high number of radiating elements would require 62 asymmetrical 1-to-2-way power dividers to synthesize the desired excitation profile. This approach would increase dramatically the complexity of the design and fabrication. To overcome this challenge, a modified innovative version of the Taylor distribution is employed in our design, which keeps the SLL lower than

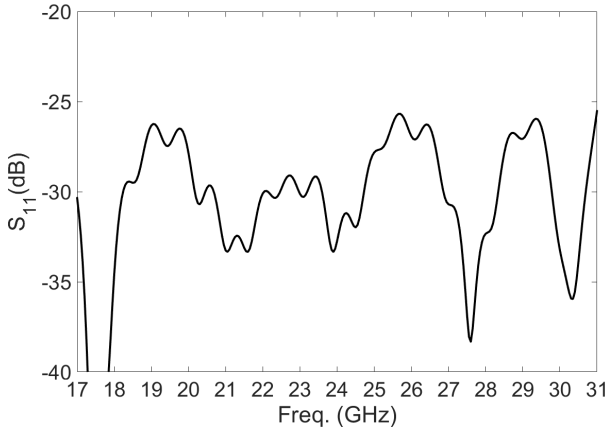

Fig. 8. Simulated reflection coefficient of the pillbox beamformer-to-CFN transition.

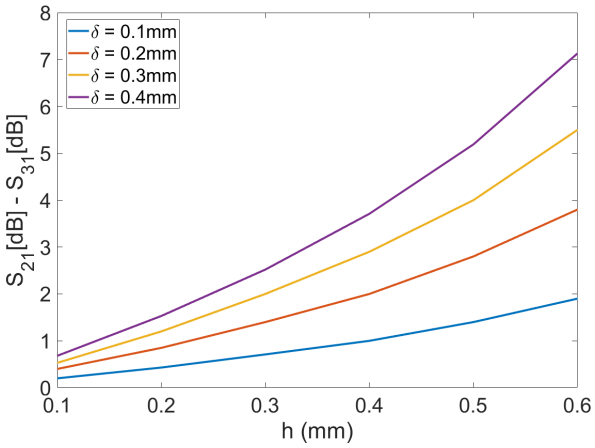

Fig. 9. Parametric study on the power division ratios between output ports at 31 GHz as a function of the design parameters for ϕ = 1.8mm in Fig. 3b.

–18 dB in both the up-link and down-link frequency bands. Specifically, the full radiating aperture is divided into 8 sets, each set consisting of 8 elements (radiating slots) excited with the same excitation factor, referred to as "octuple excitation", instead of utilizing the classical Taylor excitation. This novel technique, introduced in [35], simplifies the design process and reduces the number of required asymmetrical power dividers to only 6 instead of 62, replacing the rest of the unequal power dividers in the classical Taylor distribution network by equal power dividers. More details on the approach can be found in [35].

As presented in Fig. 2, the CFN and the Taylor octuple excitation aperture distribution have mirror symmetry along the antenna axis, so only one half of the CFN needs to be designed. Consequently, only three asymmetrical power dividers are designed for the CFN, and the other three are mirrored. The systems #1 to #4 represent the needed power dividers to implement the CFN. For a –23 dB SLL at 31 GHz, the power division ratios for systems #2, #3.1, and #3.2 in Fig. 2 are 6 dB, 6 dB, and 2.5 dB, respectively. Systems #1 and #4 are equal power dividers. Finally, system #5 represents the final stage on top of the CFN, which is a 4-slot long slot antenna array. Further details about this block will be provided later.

The unit cell of the asymmetrical power dividers is shown in Fig. 3b. It consists of five ISOLA Astra® MT77 substrate layers with a standard thickness of 0.76mm and 0.037mm dual-layer copper sheets. The bonding films between the substrates are Rogers CuClad 6250 (ϵ_r = 2.32 and tan δ = 0.0013 @ 10 GHz). After assembly, each film's pressed thickness is estimated to 0.02mm [36]. Using a 0.02mm bonding film limits the power leakage between each two substrate layers to about 0.15 dB. For a 5-layer system, this will negatively impact the total power radiated by the antenna. It should also be mentioned that reducing the number of layers to reduce the leakage will degrade the reflection coefficient, and limit the power division ratio and its stability. This is the second critical challenge in the implementation of the CFN. A contactless transition inspired from [37] has been used to reduce this loss to less than 0.1 dB for the full 5-layer system. Such a transition consists of slots etched at approximately a quarter guided wavelength at the center frequency from the unit cell central axis as shown in Fig. 3b. These slots behave as a choke to prevent leakage in the prepreg layers. The etching process for the side slots is standard in PCB technology, and replaces the need for thru/blind vias, which can be a very complicated and expensive process to provide electrical contact between the various layers.

The blind via in the top layer of Fig. 3b represents the main difference between the equal and unequal power dividers. By controlling its depth (h), diameter (ϕ), and position (δ), the power division ratio between the output ports can be manipulated. A parametric study has been conducted on the depth h and the position δ of this blind via for a diameter ϕ of 1.8mm at 31 GHz, and its results reported in Fig. 9. As observed, the power division ratio between the output ports increases with the position δ of the blind via or its depth h, or both. However, the matching levels will deteriorate and the phase difference between the output ports will change as well. To improve both, the lengths and offsets of the coupling slots are further engineered. The blind via is not necessary for equal power divisions. The lateral walls of the integrated PPW are made by vias with 0.6mm diameter, and 1.2mm for their periodicity. The blind via has a pitch of 2.4mm along the y-axis. The widths between any two rows of vias (referred to by 'W' in Fig. 3b) are limited by a maximum of $\lambda_0/4$, following the guidelines in [16], [38], where λ_0 is the wavelength at 31 GHz. The final optimized dimensions for the systems from 1 to 4 are reported in Table I. It should be noted that systems #2 and #3.1 are different as system #2 is the most critical. Indeed it requires to exhibit a high power division ratio of 4 dB across the full band for the SLL to remain below –18 dB.

All four systems from system #1 to system #4 have been optimized, and their numerical results are reported in Fig. 10. The reflection coefficients are better than –25 dB and the power division ratios are stable across the whole band. The phase difference between the output ports is less than

TABLE I
DIMENSIONS OF THE POWER DIVIDERS IN MILLIMETERS.

Design Symbols	Systems #1, #4	System #2	System #3.1	System #3.2
W_1, W_2	1.2, 1.5	1, 1.2	1.2, 1.2	1.2, 1.3
W_3, W_4	1.9, 2.1	1.5, 1.4	1.4, 1.3	1.3, 1.3
δ, ϕ, h	–	0.28, 1.8, 0.6	0.35, 1.8, 0.5	0.13, 1.8, 0.4
d, l	0.5, 2.75	0.5, 2.75	0.5, 2.75	0.5, 2.75

10° (nearly $0.16\lambda_g$ where λ_g is the guided wavelength in the substrate at 31 GHz) across a 55% bandwidth. It is important to mention that there is a ±0.1mm fabrication tolerance error to the position of the blind via (δ). Such a tolerance can affect the power division ratio by a ±2 dB than intended (as shown in Fig. 9). This tolerance is considered in the designing procedure and the selected power division ratios ensure the SLL is always better than –18 dB across the full band with different fabrication tolerances.

D. Stair Transition

An innovative solution entitled "stair transition" is introduced to fold the CFN and the pillbox beamformer transition into 7 substrate layers with no effect on neither the bandwidth, nor on its behaviour as a true time delay network. To explain this new concept, let us consider the system in Fig. 11a. It resembles a 1-to-4 power divider. A 1-to-4 power divider is then implemented in two stages. The first stage is one 1-to-2 power divider. The second stage connects each output of the previous stage with another similar 1-to-2 power divider. The total number of layers in this case is 5 layers. A general formula that calculates the number of layers for any number of stages is

$$N_l = S \times (N_p - 1) + 1. \quad (1)$$

where N_l is the total number of layers, S is the number of stages of the power division based on 1-to-2 power dividers, and N_p is the number of layers per power divider, assuming the number of layers for each power divider is the same for any stage. Applying this formula to our case, given we have 5 layers per each power divider, and 4 stages in total (from system #1 to system #4), the total number of required layers becomes 17. When we add the extra 4 layers needed for the transition between the pillbox and the CFN, a total number of 20 layers is required for the entire CFN. Now, let us apply the new solution presented in Fig. 11b. In this case, the first power divider is implemented as shown in the previous section, namely by transferring the guided mode vertically between the various stages of the power divider. Afterwards, we couple the output power to the lowest possible substrate layer in the stack-up. This technique reduces the number of needed layers in Fig. 11a to 4 instead of 5. By applying the same concept again to the output of the two 1-to-2 power dividers, cascading another stage will require only 1 substrate layer. Therefore, the required number of substrate layers becomes

$$N_l = S + N_p - 1. \quad (2)$$

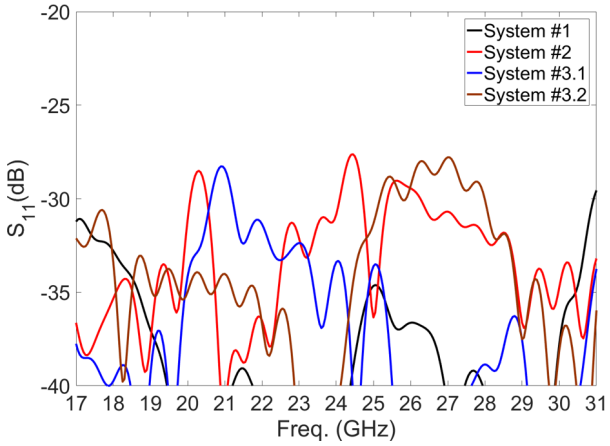

(a)

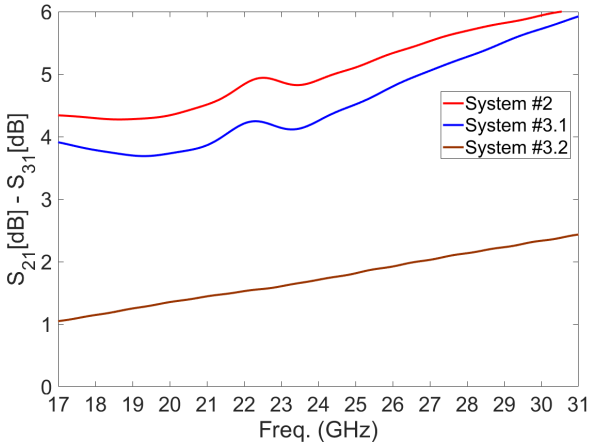

(b)

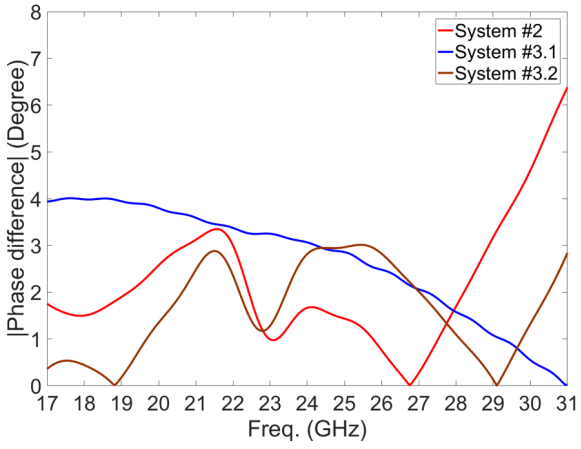

(c)

Fig. 10. Simulated results for the equal and unequal power dividers. (a) Reflection coefficients. (b) Power division ratios. (c) Phase difference between output ports.

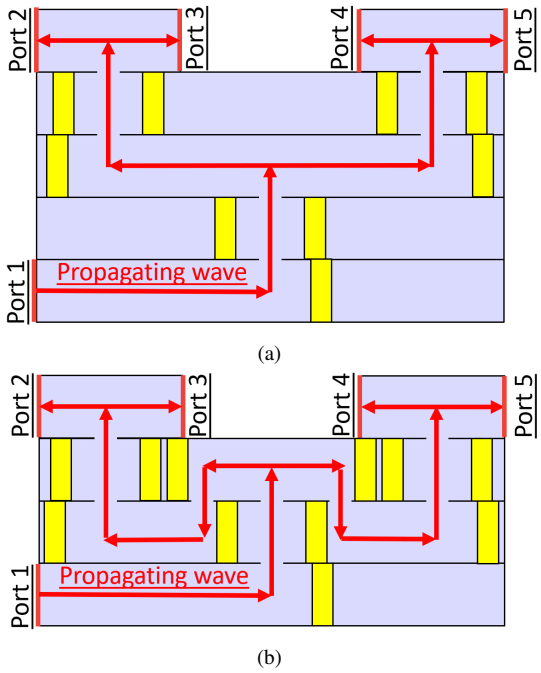

Fig. 11. 1-to-4 power divider. (a) Standard implementation. (b) Folded implementation using the in "stair transition".

Applying this formula to our system, the number of layers for the 4-stage CFN is reduced from 17 to merely 8 (excluding the pillbox beamformer-to-CFN transition layers). This is more than 50% reduction. The stair transition needed in this case should couple the power in the power divider from the 5th substrate layer (its 2 output ports) to the 2nd substrate layer (one layer above the input). This system is referred to as subsystem #1.1 in Fig. 2, and is shown in Fig. 3c. Moreover, the same stair transition system can now be applied to the transition from the pillbox beamformer-to-CFN in PCB. The output power in the 4th substrate layer in Fig. 3b is coupled directly to the 1st substrate layer. This way, the 4-substrate layers of the pillbox beamformer-to-CFN are fully folded within the CFN with a 100% compression ratio. Finally, as the integration between the pillbox beamformer-to-CFN transition, and the 5-layer equal power divider (system #1 in Fig. 2) leaves most of the power concentrated in a small path in the 1st substrate layer, another stair transition can be implemented to couple the power from the 5th substrate layer to the 1st layer, instead of the 2nd one, folding the system even further. This system is referred to as subsystem #1.2 in Fig. 2, and is shown in Fig. 3d. This increases the total compression ratio to 65%, as only 7 layers are used to build the full system so far instead of 20.

Both stair systems reflection coefficients are reported in Fig. 12. The simulated results show reflection coefficients better than –35 dB across the full frequency bands. The insertion loss is less than 0.1 dB (not shown for brevity). The integration of both presented stair transitions with the pillbox beamformer-to-CFN transition and the equal power divider denoted as system #1 is shown in Fig. 13. It is very worth mentioning that following this concept, an increment in the number of slots from 64 to 128 will only increase the number of substrate layers by one, but doubling the directivity of the antenna.

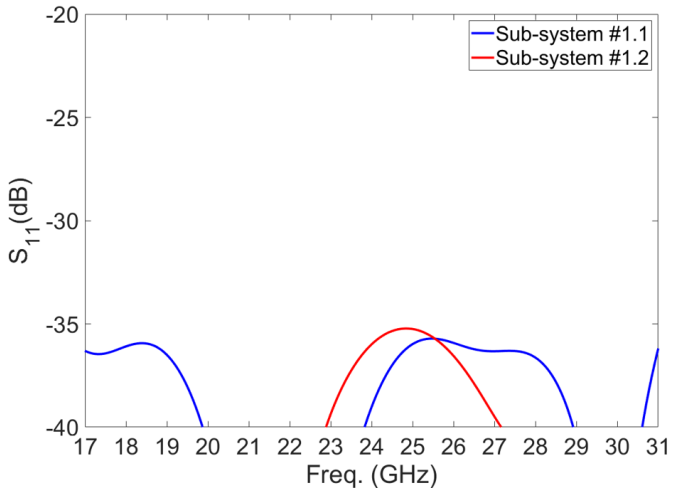

Fig. 12. Reflection coefficient of the stair transition for the two sub-systems used in the antenna.

E. Radiating Unit Cell

The radiating unit cell for the 4-slot sub-block is presented as system #5 in Fig. 2 and depicted in Fig. 3e. The design of this unit cell is accomplished in two stages. Firstly, a unit cell with 2 slots is optimized to achieve a reflection coefficient better than –15 dB from 17 GHz to 31 GHz. The unit cell is constructed using 6 substrate layers of 0.51mm thickness, which is a new thickness optimized to maximize the bandwidth of the unit cell. An additional 1mm thick layer is added on top of the radiating unit cell for matching purposes [39]. Periodic boundary conditions are employed to simulate the 64-slot array. To account for the reduced substrate thickness, new parameters are adopted for the vias, with a diameter of 0.4mm and a pitch of 0.8mm. The periodicity between the 2 slots is set at 4.7mm ($\lambda_0/2$).

In the second stage, the unit cell is integrated with an equal 1-to-2 way power divider. An equal power divider, as presented in subsection II-C, cannot be used, as the long slot unit cell has a different substrate thickness of 0.51mm. Instead, a 3-layer equal power divider is designed and combined with the small long slot unit cell.

Both systems demonstrate a reflection coefficient better than –15 dB (not shown for brevity). It should be noted that the "stair transition" employed in earlier stages cannot be fully utilized for the long slot unit cell due to the high-density of power dividers near the top stages of the CFN, leaving no space for its incorporation.

III. Simulated and Measured Results

Simulating the entire antenna would require huge computing power due to its large electrical size and complexity. To overcome this limitation, the authors conducted two separate simulations. The first simulation considered a 2.4mm slice of the cascaded system from the pillbox dual 90° symmetrical

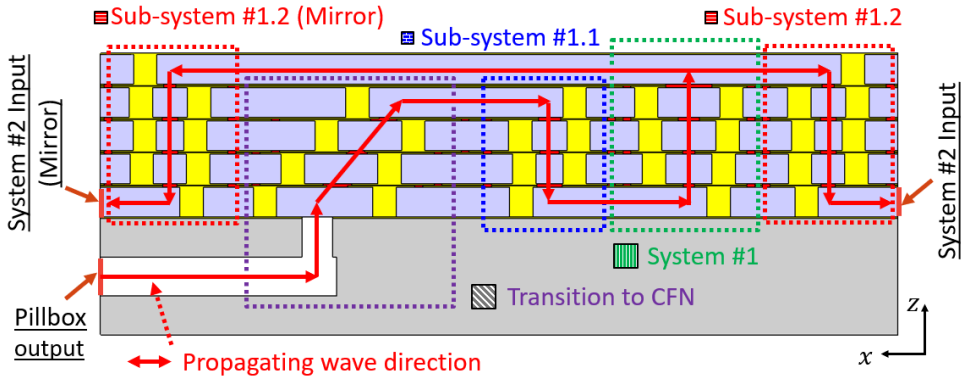

Fig. 13. Cascaded systems from the pillbox beamformer output to the input port of System #2 input.

TABLE II
PROPOSED LONG SLOT ANTENNA ARRAY PERFORMANCE METRICS.

Operation band	Down-link			Up-link		
Freq. (GHz)	**17**	**19.5**	**21.5**	**27.5**	**29**	**31**
Directivity (dBi)	34.6	34.8	37	38.6	38.9	38.7
Real. gain (dBi)	30.8	30.8	32.5	32.7	32.4	30.8
Aper. efficiency (%)	56	44	61	54	51	43

(a) Top view. (b) Side view.

Fig. 14. Fabricated prototype.

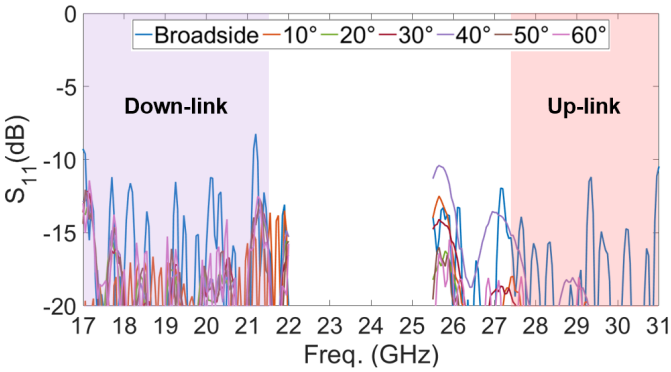

Fig. 15. Measured reflection coefficient at different scanning angles across down-link and up-link frequency bands.

bends to the 64-slot antenna array. This represents the system shown in Fig. 4 under periodic boundary conditions along the zx-plane (without the feeding horn). Radiation boundary conditions are applied otherwise. The objective of this simulation was to ensure that the reflection coefficient was better than –10 dB across the full band and to validate the tapering procedure, as well as its impact on the far-field radiation patterns in the azimuth plane (E-plane or zx-plane in Fig. 1). The second simulation involved only the pillbox beamformer (as it is shown in Fig. 5) without any connection to the CFN and the long slot array to retrieve the far-field radiation patterns in the zy-plane. Ansys. HFSS was used for this simulation [40]. In this case, perfect electric conductor (PEC) boundary conditions are applied to the pillbox beamformer except to the output PPW in the upper layer. Instead, it is terminated by a perfectly matched layer (PML) boundary condition. The corresponding far-field radiation patterns at broadside can be automatically calculated. The reflection coefficients achieved for both systems (the long slot radiating aperture with the tapered CFN, and the pillbox beamformer) in the up-link and down-link frequency bands were better than –13 dB. Moreover, the frequency band from 17 GHz to 31 GHz is fully covered with a reflection coefficient better than –10 dB. This represents a 55% bandwidth. Furthermore, both systems exhibited a SLL better than –18 dB at broadside. The half-power beam-width (HPBW) ranged from 3.5° to 2.2° in the E-plane and from 2.8° to 2.3° in the H-plane from 17 GHz to 31 GHz, respectively. As the far-field radiation patterns of the pillbox beamformer are orthogonal to those of the long slot antenna array, the far-field radiation patterns in the E-plane are expected to remain unchanged when scanning along the H-plane.

The fabricated prototype is shown in Fig. 14. The antenna was characterized at IETR, Rennes, France. The full profile of the antenna measures 4.2cm (equivalent to $4.3\lambda_0$). The metallic parts comprise the pillbox beamformer, upon which our proposed CFN and long slot antenna array in PCB are mounted. The reflection coefficients of the antenna were measured under broadside radiation and different scanning angles from 10° to 60° with a 10° step using standard waveguides WR51 and WR28 and are presented in Fig. 15. Note that the reflection coefficient is provided in the operating bands of the two used waveguides, the reflection coefficients from 22 GHz to 25.5 GHz are not measured. However, across the up-link and down-link bands, the reflection coefficient remains mostly below –10 dB for broadside radiation, and fully under –11 dB for all scanning angles up to 60°. Higher values are observed for broadside radiation for which higher reflections are generally observed for systems fed by pillbox transitions.

We report the measured 2-D far-field radiation patterns in

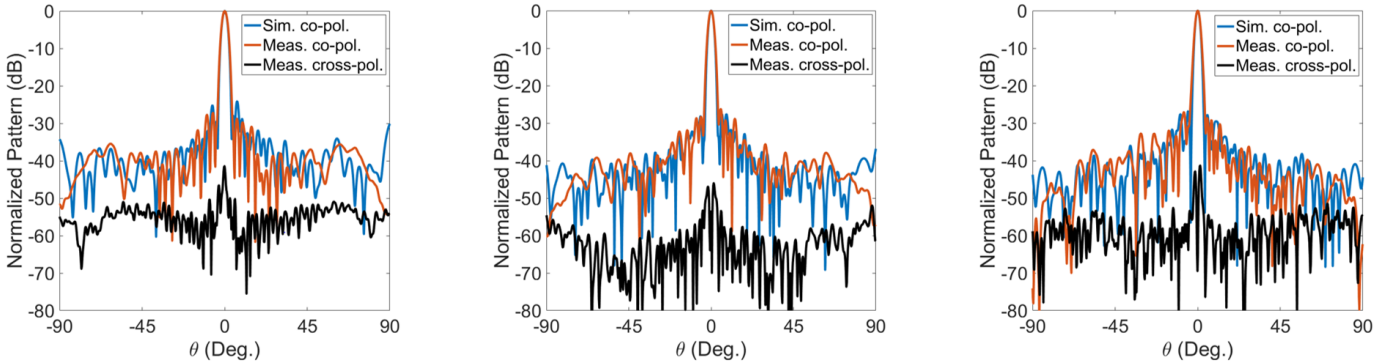

(a) 17 GHz. (b) 19.5 GHz. (c) 21.5 GHz.

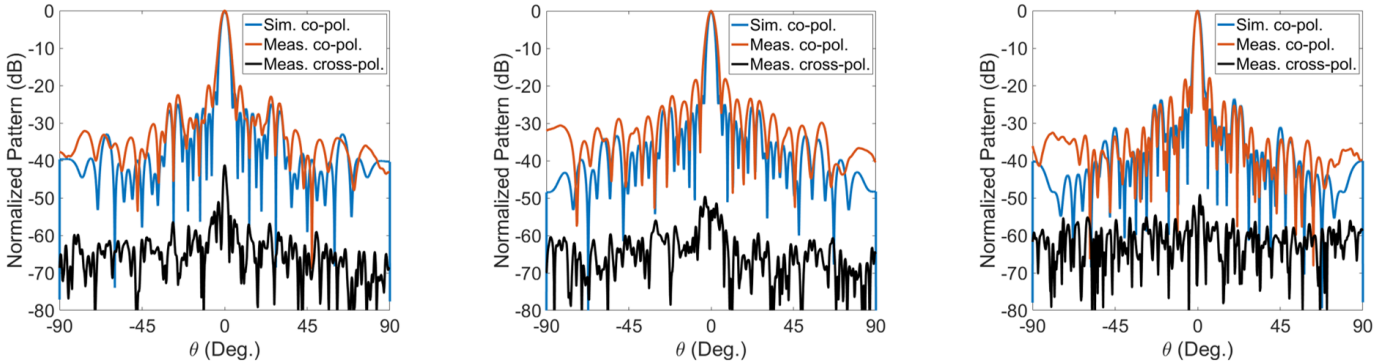

(d) 17 GHz. (e) 19.5 GHz. (f) 21.5 GHz.

Fig. 16. Measured co-pol and cross-pol far-field radiation patterns in the down-link frequency band at three frequency points (17 GHz, 19.5 GHz, and 21.5 GHz). (a-c) Broadside H-plane. (d-f) Broadside E-plane.

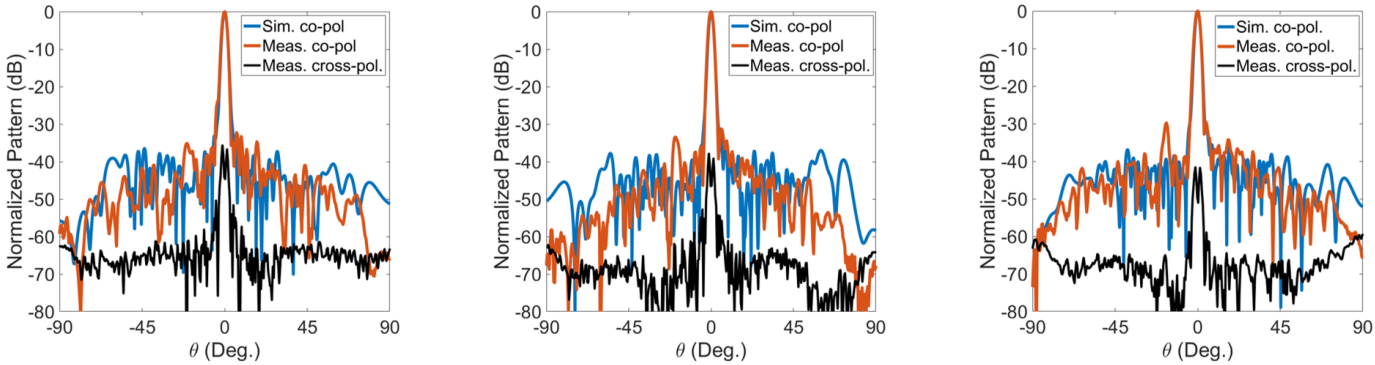

(a) 27.5 GHz. (b) 29 GHz. (c) 31 GHz.

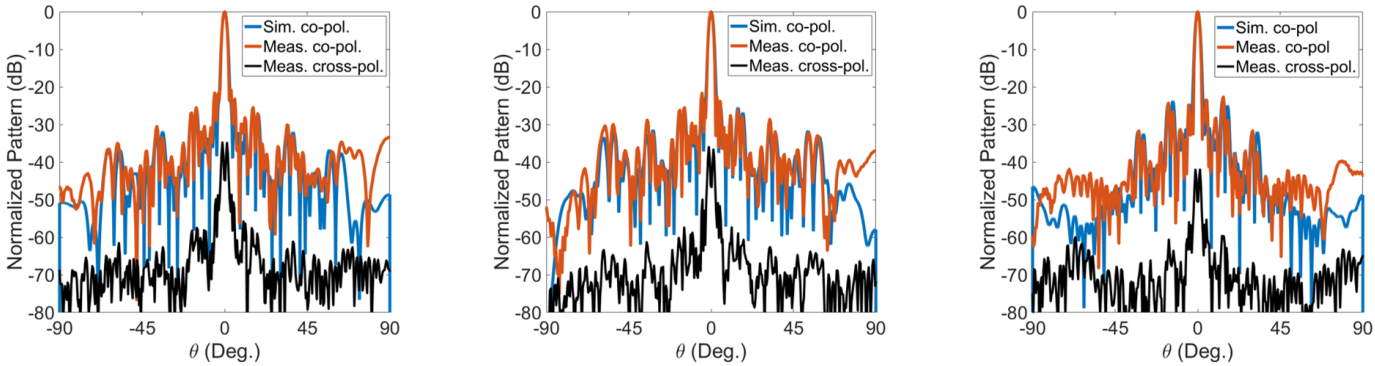

(d) 27.5 GHz. (e) 29 GHz. (f) 31 GHz.

Fig. 17. Measured co-pol and cross-pol far-field radiation patterns in the down-link frequency band at three frequency points (27.5 GHz, 29 GHz, and 31 GHz). (a-c) Broadside H-plane. (d-f) Broadside E-plane.

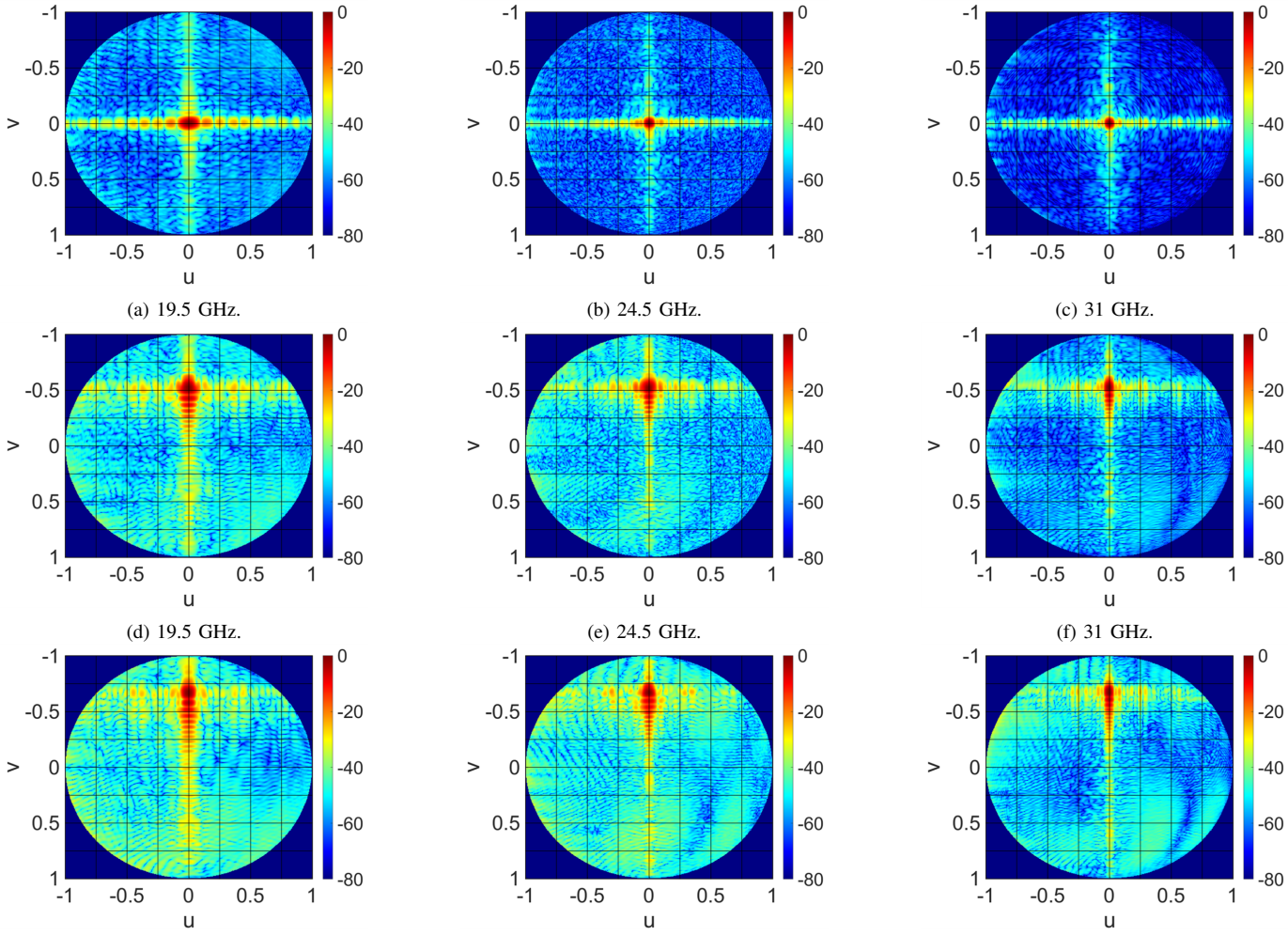

(a) 19.5 GHz. (b) 24.5 GHz. (c) 31 GHz.

(d) 19.5 GHz. (e) 24.5 GHz. (f) 31 GHz.

(g) 19.5 GHz. (h) 24.5 GHz. (i) 31 GHz.

Fig. 18. Measured far-field radiation patterns at 19.5 GHz, 24.5 GHz, and 29 GHz. H-plane horn is located at (a-c) Broadside. (d-f) 110mm to scan at 31°. (g-i) 150mm to scan at 42°.

TABLE III
COMPARISON TO STATE-OF-THE-ART LINEARLY-POLARIZED LONG SLOT ANTENNA ARRAYS.

Ref.	Number of bands‡	Center Freq. (GHz) / Full BW (%)	Fabrication technology	Num. of stubs	Thickness ($\lambda_{\min.}$)	Min. Gain (dBi)	SLL (dB)§	Min. Aper. Efficiency
[13]	Single band	27 / 18.2	PCB	8	0.53	27.6	–13	60
[14]	Single band	29 / 12	CNC milling	16	4.3	29	–13	–
[15]	Triple band	13 / 28.6 20 / 21.7 30 / 15.1	CNC milling	16	5.2	24.2	–13.2	41
[16]	Dual band Broadband	20 / 12.3, 29 / 12 25 / 50	PCB	8	0.3	16.5	–13.2	–
[41]	Dual band	77.6 / 3.4 89.7 / 14.5	PCB	15	0.4	25.3	–13.3	39.54
[42]	Dual band	19.8 / 3 29.3 / 2.7	PCB	15	0.97	24.2	–9	19.74
[43]	Single band	78.5 / 8.8	CNC milling & PCB	32	8.8	29.3	–13	38
[44]	Single band	60 / 25.2	Low Temperature Co-Fired Ceramic (LTCC)	4	0.9	14.25	–13.5	–
[45]	Single band	33 / 42.4	CNC milling	16	2.8	26.8	–13.3	75
[46]	Single band	20.5 / 32.6	PCB	8	0.53	19.2	–13	–
This work	Dual band Broadband	19.5 / 23.4, 29 / 12 24.5 / 55	CNC milling & PCB	64	4.3	30.9	–18	44

‡ This field represents only the highlighted band in the reference and not the full band of the antenna.
§ This field represents the SLL measured at broadside.

the sub-frequency bands: the down-link (17 GHz to 21.5 GHz) and the up-link (27.5 GHz to 31 GHz). Each frequency band is sampled with a 0.5 GHz frequency step. The radiation patterns of the down-link frequency band, namely 17 GHz, 19.5 GHz, and 21.5 GHz, are shown in Fig. 16. For the H-plane, the measurements closely align with full-wave simulations, with SLLs below –24 dB and HPBWs almost identical to the simulations. In the E-plane, the SLLs are below –18 dB, proving the validity of the proposed tapering procedure, although there is a slight increase in the HPBW and the SLL compared to simulations. This can be attributed to extra losses in the substrates, bonding layers, and metallized copper sheets, as well as fabrication tolerances that can affect the tapering profile.

As for the up-link frequency band, another set of three frequency points (27.5 GHz, 29 GHz, and 31 GHz) has been selected to demonstrate the antenna performance. The measured far-field radiation patterns are shown in Fig. 17. The H-plane shows consistency across the full frequency band with SLL below –24 dB and HPBWs similar to simulations. In the E-plane, the SLLs are below –20 dB, better than the down-link. These results demonstrate again the validity of the applied tapering process in providing SLLs better than –18 dB across the full band as previously discussed in Section II-C. The cross-polarization levels in both bands are less than –40 dB.

Furthermore, the directivity and the realized gain of the antenna are measured at broadside for the down-link and the up-link frequency bands. Each band is sampled by 3 frequency points as presented before. The results are reported in Table II. The antenna shows a maximum directivity of nearly 39 dBi at 29 GHz. The realized gain is always greater than 30.8 dBi for the full band. The aperture efficiency has been derived by considering a radiating surface equal to $315\times406\text{mm}^2$ and also reported in Table II. The aperture efficiency is greater than 44% across the full band.

To demonstrate the very broadband properties of the proposed antenna and its stability with beam scanning, we present complete 3-D plots of the normalized measured electric field in the upper half hemisphere of the antenna. In order to present the angular distribution of the far-field radiation patterns from the antenna's Cartesian coordinates, we have transformed our data into the normalized uv-plane ($u = \sin\theta.\cos\phi, v = \sin\theta.\sin\phi$ as defined in Fig. 1). We present in Fig. 18 our results at 19 GHz, 24.5 GHz, and 29 GHz for three main beam directions (broadside, 31°, and 42°). The scanning angle can be simply controlled by moving the feeding horn along the focal line of the parabolic reflector of the pillbox coupler. The two scanning angles can be obtained by displacing the horn by 110mm and 150mm, respectively. At broadside, it can be seen clearly that the power is very well collimated. For both scanning angles, the pointing directions are very stable across the full frequency band. The SLL across the E-plane is stable, and we expect the same stable behavior up to a scanning angle of 60° [47]. The SLL across the H-plane increases with the increase in scanning angle. Large steering angles may cause distortion in the far-field radiation pattern and multiple reflections due to the nature of the designed pillbox coupler. These issues can be resolved by increasing the focal to diameter ratio of the pillbox coupler and implementing a dual-lens quasi-optical beamformer or a reflective Luneburg lens, as discussed in [19], [20], [48], [49]. However, such systems are not the focus of this paper, but can be considered in future versions of the proposed system.

Table III compares the state-of-the-art long slot antenna array in literature. Our proposed prototype excels in providing a high gain and low SLL for Satcom applications in K/Ka bands and provides the widest band reported in literature with a single radiating aperture. The antenna is fabricated in standard fabrication technologies suitable for mass production.

IV. CONCLUSIONS

This article has presented an ultra-low-profile array with 64 radiating long slots realized in multilayer PCB technology with 15 dielectric substrates. The antenna operates in linear polarization over a very wide bandwidth 17–31 GHz, with stable pointing directions within the operating band. Beam steering is enabled along the H-plane up to ±42°, by means of a pillbox quasi-optical beamformer. The long slot array and CFN are made in PCB technology whereas the pillbox beamformer by CNC milling. Additionally, an innovative "stair transition" concept has been introduced to fold the CFN by 65%, reducing the profile, mass and fabrication costs. The proposed antenna is considered a suitable candidate for next generation terminal antennas for Satcom applications.

ACKNOWLEDGMENT

This work has been carried out at IETR, when Adham Mahmoud was with the University of Rennes. This publication is supported by the European Union through the European Regional Development Fund (ERDF), and by the French region of Brittany, Ministry of Higher Education and Research, Rennes Métropole and Conseil Départemental 35, through the CPER Project SOPHIE / STIC & Ondes and by CNRS. The authors would like to thank Xavier Morvan for the fabrication of CNC parts of the prototype and Laurent Le Coq for performing measurements.

REFERENCES

[1] H. Fenech, S. Amos, A. Tomatis, and V. Soumpholphakdy, "High throughput satellite systems: An analytical approach," *IEEE Trans. Aero. Elect. Systems*, vol. 51, no. 1, pp. 192–202, 2015.

[2] A. J. Roumeliotis, C. I. Kourogiorgas, and A. D. Panagopoulos, "Optimal dynamic capacity allocation for high throughput satellite communications systems," *IEEE Wireless Comm. Lett.*, vol. 8, no. 2, pp. 596–599, 2019.

[3] S. Mercader-Pellicer, F. Rigobello, G. Goussetis, L. Dufour, D. Bresciani, H. Legay, and N. J. G. Fonseca, "Dual Ka-band multiple beam reflector antenna for western european coverage," in *Europ. Conf. Ant. Prop. (EuCAP)*, pp. 1–4, 2019.

[4] G. Mishra and S. K. Sharma, "Ka-band offset spherical reflector antenna fed by dual-cp horn array with switched multiple-beams," in *IEEE Radio Wireless Symp. (RWS)*, pp. 36–38, 2021.

[5] S. A. Matos, E. B. Lima, J. S. Silva, J. R. Costa, C. A. Fernandes, N. J. G. Fonseca, and J. R. Mosig, "High gain dual-band beam-steering transmit array for satcom terminals at Ka-band," *IEEE Trans. Antennas Propag.*, vol. 65, no. 7, pp. 3528–3539, 2017.

[6] K. T. Pham, R. Sauleau, E. Fourn, F. Diaby, A. Clemente, and L. Dussopt, "Dual-band transmitarrays with dual-linear polarization at Ka-band," *IEEE Trans. Antennas Propag.*, vol. 65, no. 12, pp. 7009–7018, 2017.

[7] J. I. Herranz-Herruzo, A. Valero-Nogueira, M. Ferrando-Rocher, B. Bernardo, A. Vila, and R. Lenormand, "Low-cost Ka-band switchable RHCP/LHCP antenna array for mobile SATCOM terminal," *IEEE Trans. Antennas Propag.*, vol. 66, no. 5, pp. 2661–2666, 2018.

[8] G. Gültepe, T. Kanar, S. Zihir, and G. M. Rebeiz, "A 1024-element Ku-band SATCOM dual-polarized receiver with >10-db/k G/T and embedded transmit rejection filter," *IEEE Trans. Microwave Theory Tech.*, vol. 69, no. 7, pp. 3484–3495, 2021.

[9] K. K. W. Low, S. Zihir, T. Kanar, and G. M. Rebeiz, "A 27–31-GHz 1024-element Ka-band SATCOM phased-array transmitter with 49.5-dBW peak EIRP, 1-db AR, and ±70° beam scanning," *IEEE Trans. Microwave Theory Tech.*, vol. 70, no. 3, pp. 1757–1768, 2022.

[10] W. M. Abdel-Wahab, H. Al-Saedi, E. H. Mirza Alian, M. Raeis-Zadeh, A. Ehsandar, A. Palizban, N. Ghafarian, G. Chen, H. Gharaee, M. R. Nezhad-Ahmadi, and S. Safavi Naeini, "A modular architecture for wide scan angle phased array antenna for K/Ka mobile SATCOM," in *IEEE MTT-S International Micro. Symp. (IMS)*, pp. 1076–1079, 2019.

[11] A. Mahmoud, M. Del Mastro, T. Potelon, R. Sauleau, and M. Ettorre, "Mutli-layer CTS antenna array in PCB technology for SatCom applications," in *Micro. Med. Sym. (MMS)*, pp. 1–3, 2022.

[12] X. Lu, S. Gu, X. Wang, H. Liu, and W. Lu, "Beam-scanning continuous transverse stub antenna fed by a ridged waveguide slot array," *IEEE Ant. Wireless Prop. Lett.*, vol. 16, pp. 1675–1678, 2017.

[13] Y. Lu, Q. You, Y. Wang, Y. You, J. Huang, and K. Wu, "Millimeter-wave low-profile continuous transverse stub arrays with novel linear source generators," *IEEE Trans. Antennas Propag.*, vol. 67, no. 2, pp. 988–997, 2019.

[14] M. Ettorre, F. F. Manzillo, M. Casaletti, R. Sauleau, L. Le Coq, and N. Capet, "Continuous transverse stub array for Ka-band applications," *IEEE Trans. Antennas Propag.*, vol. 63, no. 11, pp. 4792–4800, 2015.

[15] Q. You, Y. Lu, Y. Wang, J. Xu, J. Huang, and W. Hong, "Hollow-waveguide tri-band shared-aperture full-corporate-feed continuous transverse stub antenna," *IEEE Trans. Antennas Propag.*, vol. 70, no. 8, pp. 6635–6645, 2022.

[16] M. Del Mastro, A. Mahmoud, T. Potelon, R. Sauleau, G. Quagliaro, A. Grbic, and M. Ettorre, "Ultra-low-profile continuous transverse stub array for SatCom applications," *IEEE Trans. Antennas Propag.*, vol. 70, no. 6, pp. 4459–4471, 2022.

[17] J. Ji, C. Wang, X. Wu, and J. Zhou, "A K/Ka dual-band continuous transverse stub (CTS) antenna array with sidelobe suppression," in *2020 IEEE International Symposium on Antennas and Propagation and North American Radio Science Meeting*, pp. 3–4, 2020.

[18] M. Ettorre, R. Sauleau, and L. Le Coq, "Multi-beam multi-layer leaky-wave SIW pillbox antenna for millimeter-wave applications," *IEEE Trans. Antennas Propag.*, vol. 59, no. 4, pp. 1093–1100, 2011.

[19] J. Ruiz-García, E. Martini, C. D. Giovampaola, D. González-Ovejero, and S. Maci, "Reflecting luneburg lenses," *IEEE Trans. Antennas Propag.*, vol. 69, no. 7, pp. 3924–3935, 2021.

[20] T. Ströber, S. Tubau, E. Girard, H. Legay, G. Goussetis, and M. Ettorre, "Shaped parallel-plate lens for mechanical wide-angle beam steering," *IEEE Trans. Antennas Propag.*, vol. 69, no. 12, pp. 8158–8169, 2021.

[21] M. Śmierzchalski, F. F. Manzillo, M. D. Mastro, N. Capet, B. Palacin, R. Sauleau, and M. Ettorre, "A novel dual-polarized continuous transverse stub antenna based on corrugated waveguides—part I: Principle of operation and design," *IEEE Trans. Antennas Propag.*, vol. 69, no. 3, pp. 1302–1312, 2021.

[22] S. Lenzini, M. Del Mastro, L. Vincetti, and M. Ettorre, "Circularly-polarized CTS array antenna for SatCom applications," in *International Symp. Antennas Prop. (ISAP)*, pp. 591–592, 2021.

[23] M. Śmierzchalski, F. F. Manzillo, M. D. Mastro, N. Capet, B. Palacin, R. Sauleau, and M. Ettorre, "A novel dual-polarized continuous transverse stub antenna based on corrugated waveguides—part II: Experimental demonstration," *IEEE Trans. Antennas Propag.*, vol. 69, no. 3, pp. 1313–1323, 2021.

[24] P. Naseri, S. A. Matos, J. R. Costa, C. A. Fernandes, and N. J. G. Fonseca, "Dual-band dual-linear-to-circular polarization converter in transmission mode application to K/Ka -band satellite communications," *IEEE Trans. Antennas Propag.*, vol. 66, no. 12, pp. 7128–7137, 2018.

[25] H. B. Wang and Y. J. Cheng, "Single-layer dual-band linear-to-circular polarization converter with wide axial ratio bandwidth and different polarization modes," *IEEE Trans. Antennas Propag.*, vol. 67, no. 6, pp. 4296–4301, 2019.

[26] M. Del Mastro, M. Ettorre, and A. Grbic, "Dual-band, orthogonally-polarized LP-to-CP converter for SatCom applications," *IEEE Trans. Antennas Propag.*, vol. 68, no. 9, pp. 6764–6776, 2020.

[27] E. Gandini, M. Ettorre, M. Casaletti, K. Tekkouk, L. Le Coq, and R. Sauleau, "SIW slotted waveguide array with pillbox transition for mechanical beam scanning," *IEEE Ant. Wireless Prop. Lett.*, vol. 11, pp. 1572–1575, 2012.

[28] S.-P. Yan, M.-H. Zhao, Y.-L. Ban, J.-W. Lian, and Z. Nie, "Dual-layer SIW multibeam pillbox antenna with reduced sidelobe level," *IEEE Ant. Wireless Prop. Lett.*, vol. 18, no. 3, pp. 541–545, 2019.

[29] K. Tekkouk, M. Ettorre, E. Gandini, and R. Sauleau, "Multibeam pillbox antenna with low sidelobe level and high-beam crossover in SIW technology using the split aperture decoupling method," *IEEE Trans. Antennas Propag.*, vol. 63, no. 11, pp. 5209–5215, 2015.

[30] CST - Computer Simulation Technology AG, "CST Studio Suite." https://www.3ds.com/products-services/simulia/products/cst-studio-suite/, 2023.

[31] F. Teberio, I. Arregui, P. Soto, M. A. G. Laso, V. E. Boria, and M. Guglielmi, "High-performance compact diplexers for Ku/K-band satellite applications," *IEEE Trans. Micro. The. Tech.*, vol. 65, no. 10, pp. 3866–3876, 2017.

[32] D. Smacchia, C. Carceller, M. Guglielmi, P. Soto, V. Boria, J. Ruiz, and P. González, "A wideband diplexer for Ka-band passive intermodulation measurement," in *IEEE MTT-S International Micro. Symp. (IMS)*, pp. 1106–1109, 2018.

[33] T. Potelon, M. Ettorre, T. Bateman, J. Francey, and R. Sauleau, "Broadband passive two-feed-per-beam pillbox architecture for high beam crossover level," *IEEE Trans. Antennas Propag.*, vol. 68, no. 1, pp. 575–580, 2020.

[34] Isola-group, "Astra® mt77." Datasheet, March 2023. https://www.isola-group.com/wp-content/uploads/data-sheets/astra-mt77.pdf.

[35] A. Mahmoud, *Flat antenna arrays for high data rate communications*. PhD thesis, Université de Rennes 1, Rennes, France, 2021.

[36] Rogers-corp., "Cuclad® 6250." Datasheet, March 2023. https://www.rogerscorp.com/advanced-electronics-solutions/cuclad-series-laminates/cuclad-6250-bonding-film.

[37] N. Capet, F. Foglia Manzillo, K. Tekkouk, R. Sauleau, and M. Ettorre, "Multilayer waveguide comprising at least one transition device between layers of this multilayer waveguide." U.S patent 9 246 232, Jan. 2016.

[38] T. Potelon, M. Ettorre, L. Le Coq, T. Bateman, J. Francey, and R. Sauleau, "Reconfigurable cts antenna fully integrated in pcb technology for 5g backhaul applications," *IEEE Trans. Antennas Propag.*, vol. 67, no. 6, pp. 3609–3618, 2019.

[39] E. Magill and H. Wheeler, "Wide-angle impedance matching of a planar array antenna by a dielectric sheet," *IEEE Trans. Ant. Prop.*, vol. 14, no. 1, pp. 49–53, 1966.

[40] "High-frequency structure simulator (HFSS)." [Computer software], 2021. Version 2021 R1.

[41] Y.-W. Wu, Z.-W. Miao, G. Q. Luo, and Z.-C. Hao, "Planar millimeter-wave shared-aperture self-diplexing antenna with small frequency ratio and high isolation," *IEEE Trans. Antennas Propag.*, vol. 69, no. 12, pp. 8979–8984, 2021.

[42] R. S. Hao, Y. J. Cheng, and Y. F. Wu, "Shared-aperture variable inclination continuous transverse stub antenna working at K- and Ka-bands for mobile satellite communication," *IEEE Trans. Antennas Propag.*, vol. 68, no. 9, pp. 6656–6666, 2020.

[43] T. Potelon, M. Ettorre, L. Le Coq, T. Bateman, J. Francey, D. Lelaidier, E. Seguenot, F. Devillers, and R. Sauleau, "A low-profile broadband 32-slot continuous transverse stub array for backhaul applications in E-band," *IEEE Trans. Antennas Propag.*, vol. 65, no. 12, pp. 6307–6316, 2017.

[44] F. Foglia Manzillo, M. Ettorre, M. S. Lahti, K. T. Kautio, D. Lelaidier, E. Seguenot, and R. Sauleau, "A multilayer LTCC solution for integrating 5G access point antenna modules," *IEEE Trans. Micro. The. Tech.*, vol. 64, no. 7, pp. 2272–2283, 2016.

[45] Q. You, Y. Lu, Y. You, Y. Wang, Z.-C. Hao, and J. Huang, "Wideband full-corporate-feed waveguide continuous transverse stub antenna array," *IEEE Access*, vol. 6, pp. 76673–76681, 2018.

[46] Y. Gao, T. Hong, W. Jiang, S. Gong, and F. Li, "Low-profile wideband CTS array using substrate-integrated waveguide technology for K-band applications," *IEEE Trans. Antennas Propag.*, vol. 67, no. 8, pp. 5711–5716, 2019.

[47] F. Foglia Manzillo, M. Ettorre, M. Casaletti, N. Capet, and R. Sauleau, "Active impedance of infinite parallel-fed continuous transverse stub arrays," *IEEE Trans. Antennas Propag.*, vol. 63, no. 7, pp. 3291–3297, 2015.

[48] L. Lassauce, J.-P. Fraysse, S. Tubau, H. Legay, and M. Ettorre, "Multi-mirror quasi-optical beamformer for wide scanning linear apertures," in *Europ. Conf. Ant. Prop. (EuCAP)*, pp. 1–3, 2023.

[49] Q. Chen, S. A. Horsley, N. J. Fonseca, T. Tyc, and O. Quevedo–Teruel, "Double-layer geodesic and gradient-index lenses," *Nat. Comm.*, vol. 13, no. 1, 2022.